Electronic Supplementary Material (ESI) for Physical Chemistry Chemical Physics.

Electronic Supplementary Information

for

Rapid Analytical CEST Spectroscopy of Competitive Host-Guest Interactions using Spatial Parallelization with a Combined Approach of Variable Flip Angle, Keyhole and Averaging (CAVKA)

Hen Amit Morik,[a,b] Patrick Schuenke[b,c] and Leif Schröder [a,b]

a. Translational Molecular Imaging, Deutsches Krebsforschungszentrum (DKFZ), Heidelberg, Germany.

b. Molecular Imaging, Leibniz-Forschungs-Institut für Molekulare Pharmakologie (FMP), Berlin, Germany.

c. Biomedical Magnetic Resonance, Physikalisch-Technische Bundesanstalt (PTB), Berlin, Germany.

SI. 1 Summation of echoes for UFZ and the challenge of fast decaying signals

a) Limits of echo summation

Döpfert et al.[1] defined a stop criterion up to which echo number the signals should be added up before further addition contributes more noise than signal increase. Echo number n with signal s_n should be added only if $s_n > \left(\sqrt{\frac{n}{n-1}} - 1\right)\sum_{i=1}^{n-1} s_i$. For exponentially decaying echoes, τ/TE is the critical parameter (τ is given by T_2 for spin echo train and by T_2^* for gradient echoes). We arbitrarily assign the first echo signal intensity $s_1 = 1$ (though this is smaller than the starting magnetization at $t = 0$). Assuming relatively slow sampling or fast decay, i.e. $TE = \tau$, then the second echo is already decayed to 36.8% of the 1st echo. The stop criterion for echo no. 2 requires that it should at least be 41.4% of the first echo to be added. Thus, $TE = \tau$ yields best signal for no further addition.

The ideal case for sampling the echoes infinitely faster than the decay means that each signal s_i contributes almost $s_i \approx 1$. The sum of the preceding n-1 echoes is (n-1) and thus the upper limit that the n-th contribution yields after normalization by the previous sum is given by $(n\text{-}1)^{-1}$. The "test criterion", shown in Fig. S1, cannot reach the yellow area but must stay outside the red area.

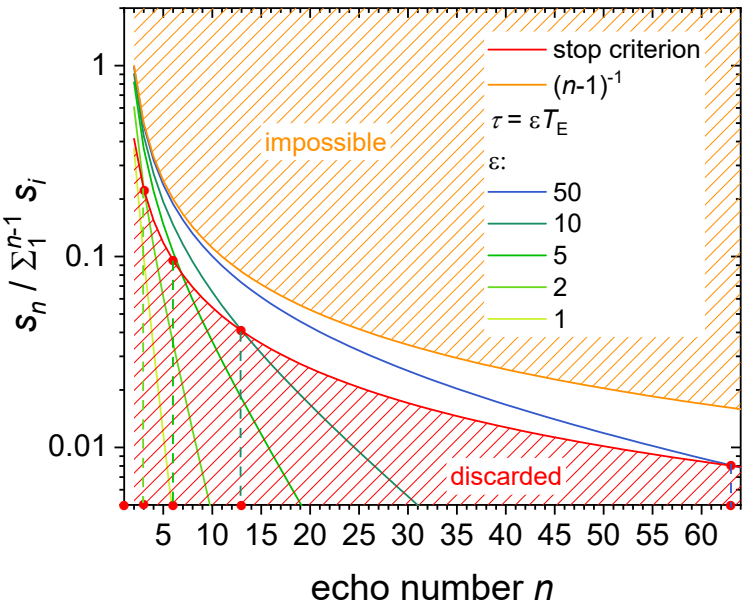

Fig. S1. Signal improvement by summation of echoes. Red area under the curve $\sqrt{n/(n-1)} - 1$ is where echo summation contributes noise rather than signal. Yellow area above the curve $1/(n-1)$ is impossible due to the non-zero scan time. Curves in green and blue with different

values of the critical parameter τ/TE intersect the red curve to show the maximal number of echoes that should be summed to improve the signal. Data is simulated.

For $\tau = 2TE$, summation up to $n = 3$ is beneficial. For $\tau = \{5; 10; 50\}TE$, summation up to $n = \{6, 13, 63\}$ improves the signal. We thus see that rapidly decaying signals like those in fast exchanging systems (τ < 10 ms for gas vesicles as seen by the FID decays in the FA calibration[2]) suffer from strong limitations with regard to efficient echo accumulation.

b) Further segmentation considerations

The profiles obtained by gradient echoes as shown by Döpfert et al. were relatively soon noise-dominated. These also showed a blurring of the sharp edges and had a small dynamic range where the Rician noise level quickly impaired the information in frequency ranges where signal loss due to CEST effect became effective.

For fast decaying signals and a low starting magnetization, there are important limitations when the available magnetization is segmented into pieces along the chemical shift dimension like in UFZ:

- only a rather small fraction of both the starting magnetization and the host actually actively participates in the CEST effect (those with the "matching" frequency along the gradient direction);
- in the typical implementation with cylindrical NMR tubes, different sections of the CEST spectrum are encoded with different reference magnetization; the shape of the reference magnetization along the spectral dimension depends on the shape of the phantom and/or the coil excitation profile along the direction of the applied gradient; low magnetizations at the edges are dominated by Rician noise, thus the "valuable" information should be concentrated towards the center;
- no redundancy in the expected data is used;
- uniform sampling is applied along the spectral dimension, thus allowing no prioritization of "important" ranges around the expected peaks.

The noise along the readout dimension after FT can be quite high for such gradient-encoded z-spectra. Contrary, the shot-to-shot noise along the chemical shift dimension for conventional CEST encoding with polarizers operated in continuous flow mode is rather low (e.g, less than 0.56% [3]). Working with natural abundance ^{129}Xe and choosing continuous flow operation has the advantage of i) being cost effective and ii) providing stable magnetization conditions over an extended period of time for comparing different spectra. It comes, however, with reduced starting magnetization (compared to enriched ^{129}Xe and cryo-separation), but this can be overcome by carefully choosing certain dimensions for signal averaging, identifying signal redundancies, and segmenting the starting magnetization i) along an "uncritical" dimension and ii) into fewer steps. It should thus be favorable to maintain step-wise (non-uniform) encoding

along $\Delta\omega$ with refreshing the magnetization for each saturation offset and implement acceleration for one of the other encoding dimensions. Instead of segmenting the magnetization into at least 64 pieces of variable amplitude along the saturation offset dimension it can be divided into 32 equal segments to optimize encoding along the spatial dimension via the VFA approach.

Along the spectral dimension, no nuclei will be affected at all by RF saturation for certain acquisitions, but for the decisive frequencies, all nuclei and hosts participate in the CEST mechanism and thus make most efficient use to encode the CEST effect even for small host concentrations. Translating the magnetization segmentation step from the chemical shift dimension (where the noise level would otherwise seriously impair the z-spectrum) into the domain of spatial frequencies (k-space) for imaging helps to spread the noise across all pixels in image space.

c) FID data to illustrate accelerated loss of phase coherence

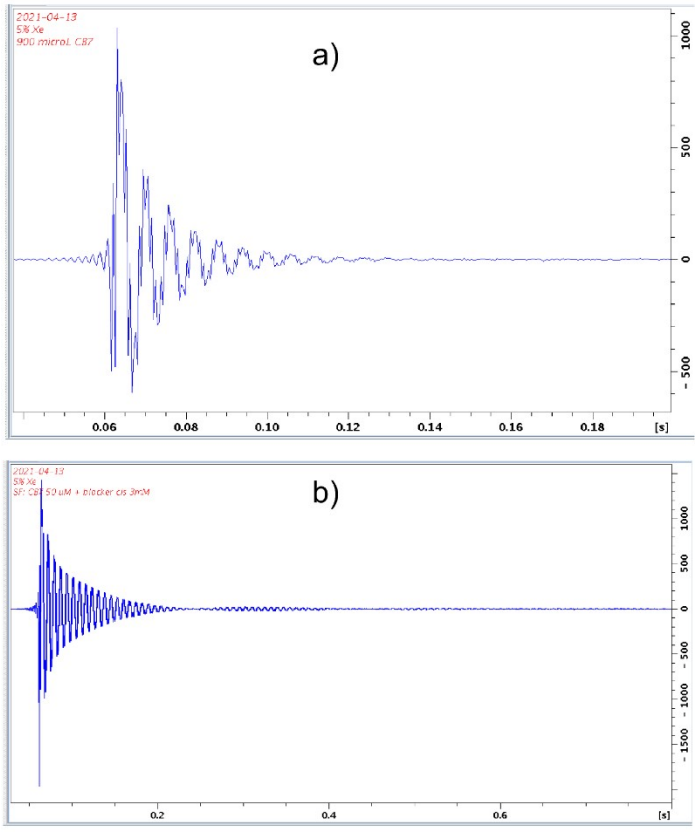

Fig. S2. The accessibility of CB7 for Xe causes an accelerated loss of phase coherence in the pool of free Xe in solution. This is illustrated by comparing the FID of two experimental conditions: a) Xe with unrestricted access to the portal/cavity and b) in the presence of the blocker **1** at 60-fold

excess. In the latter case, the FID signal lasts almost a second while in the former case, it vanishes within 180 ms.

SI. 2. The substitution factor

a) Analytical derivation

The substitution factor β scales the signal intensities in the k-space periphery to generate a smooth transition between the periphery and the keyhole region. If both the reference and the keyhole images are acquired using θ_{VFA} according to Eq. 1, which makes the transverse magnetization equal for a pre-selected number of k-space lines, the substitution factor can be derived analytically. The transverse magnetization M_{xy} in the *n*-th excitation depends on the amount of longitudinal magnetization M_z that is left from the previous excitation (*n-1*) and on the flip angle. Thus, transverse magnetization for the *n*-th k-space lines reads

$$M_{xy}(n) = M_z(n-1) \cdot \sin\left(\theta_{VFA}(n)\right), \quad n = 1, 2, \ldots, N. \tag{S1}$$

Comparing the signal in the keyhole k-space lines with the signal in the reference k-space lines yields the general form of the substitution factor

$$\beta = \frac{M_{xy}(n)_{key}}{M_{xy}(n)_{ref}}. \tag{S2}$$

Critically, when using VFA excitations, the transverse magnetizations available for each k-space lines are uniform. Thus, we can compare the signal from a single arbitrary line in the keyhole k-space to its corresponding line in the reference k-space. Choosing the first line for both k-spaces provides an elegant solution, since with substitution of $n \neq 1$ the terms would not simplify as conveniently as follows. The end result is, nonetheless, valid in general since the transverse magnetization remains constant for all lines within each dataset and can be taken from the respective first line $n = 1$. The phase encoding applied in either the fully sampled reference data or the sub-sampled keyhole causes different segmentation of the overall available magnetization but the suggested analytical scaling does not change the phase encoding rather just scales the line-wise signal magnitude. Let R be the undersampling factor (the ratio between the number of lines in the reference and keyhole k-spaces), substituting Eq. 1 and Eq. S1 into Eq. S2,

$$\beta = \frac{M_{xy}(n)_{key}}{M_{xy}(n)_{ref}} = \frac{\left(M_z(n-1)\cdot \sin\left(\theta_{VFA}(n)\right)\right)_{key}}{\left(M_z(n-1)\cdot \sin\left(\theta_{VFA}(n)\right)\right)_{ref}}$$

$$= \frac{M_z(n-1)_{key}}{M_z(n-1)_{ref}} \cdot \frac{\sin\left(\tan^{-1}\left(\frac{1}{\sqrt{N/R-n}}\right)\right)}{\sin\left(\tan^{-1}\left(\frac{1}{\sqrt{N-n}}\right)\right)}$$

$$= \frac{M_z(n-1)_{key}}{M_z(n-1)_{ref}} \cdot \frac{\frac{1}{\sqrt{N/R-n+1}}}{\frac{1}{\sqrt{N-n+1}}} \overset{n=1}{=} \frac{M_0}{M_0} \cdot \frac{\sqrt{N}}{\sqrt{N/R}} = \sqrt{R}.$$

(S3)

In this derivation, the identity $\sin\left(\tan^{-1}\left(1/\sqrt{x}\right)\right) = 1/\sqrt{x+1}$ was used and the initial longitudinal magnetization is M_0.

b) Experimental support for the analytically derived value

To validate the formula for the substitution factor (Eq. S3), we compared the predicted values with experimentally determined ones. The histograms in Fig. S3 show the pixel-wise ratios between signal intensities in the keyhole k-spaces and signal intensities in the equivalent areas in the reference k-spaces for six different undersampling factors between *R* = 1.33 (Fig. S3A) and *R* = 8 (Fig. S3F). Due to the decreasing number of pixels for increasing undersampling factors, the total number of counts varies between 576 (Fig. S3A) and 16 (Fig. S3F). Further, the different levels of transverse magnetization for different undersampling factors lead to a shift of the mode of the histograms towards higher values for higher undersampling factors. This shift clearly follows the prediction according to Eq. S3. The analytically derived substitution factors for all investigated R values (dashed orange lines in Fig. S3A-F) fit the modes of the histograms and thus the experimentally derived values very well.

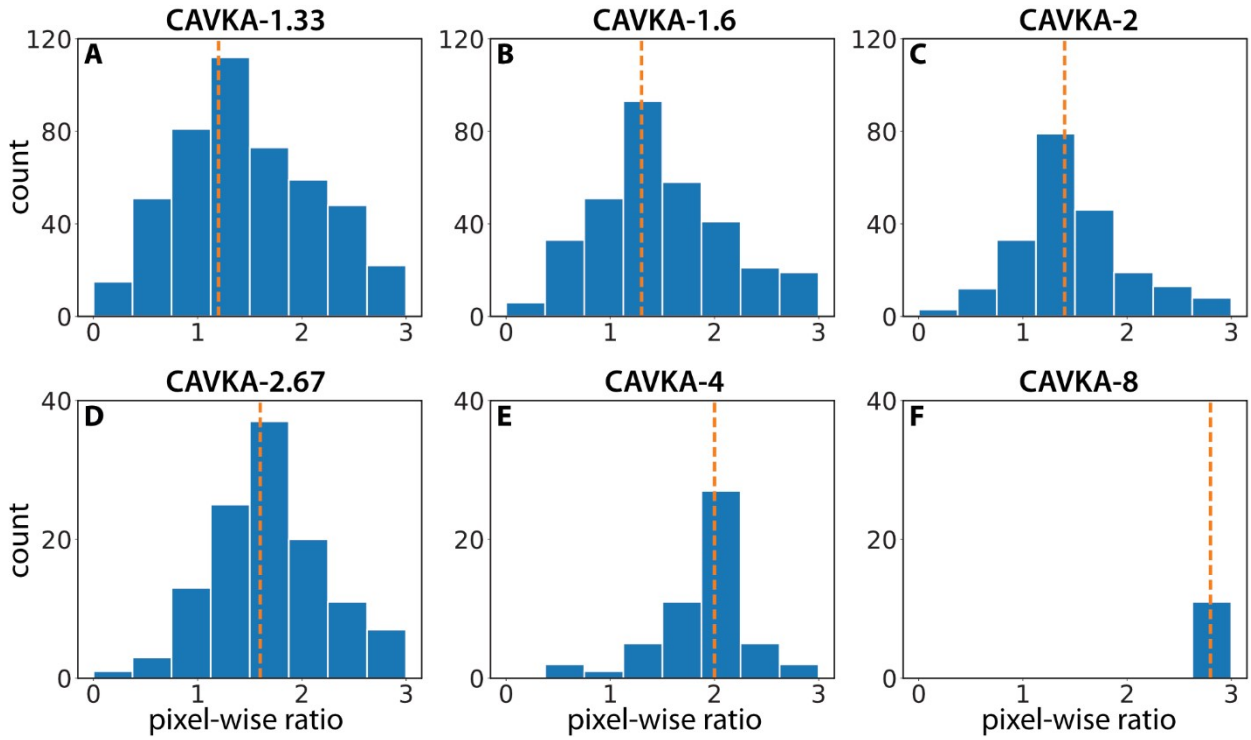

Fig. S3. Experimental validation of the analytically derived substitution factor β. The histograms show the distribution of the pixel-wise ratios between signal intensities in the keyhole k-space pixels and the signal intensities in the corresponding reference k-space pixels. The dashed orange lines illustrate the analytically derived values according to Eq. S3. For all investigated undersampling factors between $R = 1.33$ (A) and $R = 8$ (F), the modes of the histograms match the theoretical values.

c) Impact of incorrect substitution factor

The choice of the correct substitution factor minimizes distortions in the reconstructed images that result from discontinuity in the signal intensity profiles of composite k-spaces. Fig. S4 demonstrates the effect of such discontinuities. Whereas overestimated β values lead to overrepresented periphery values and thus to very noisy images (Fig. S4 middle), underestimated β values lead to an underrepresentation of high frequencies and therefore to blurring (Fig. S4, right). This blurring due to underestimated β values is comparable to the effect of zero-filling.

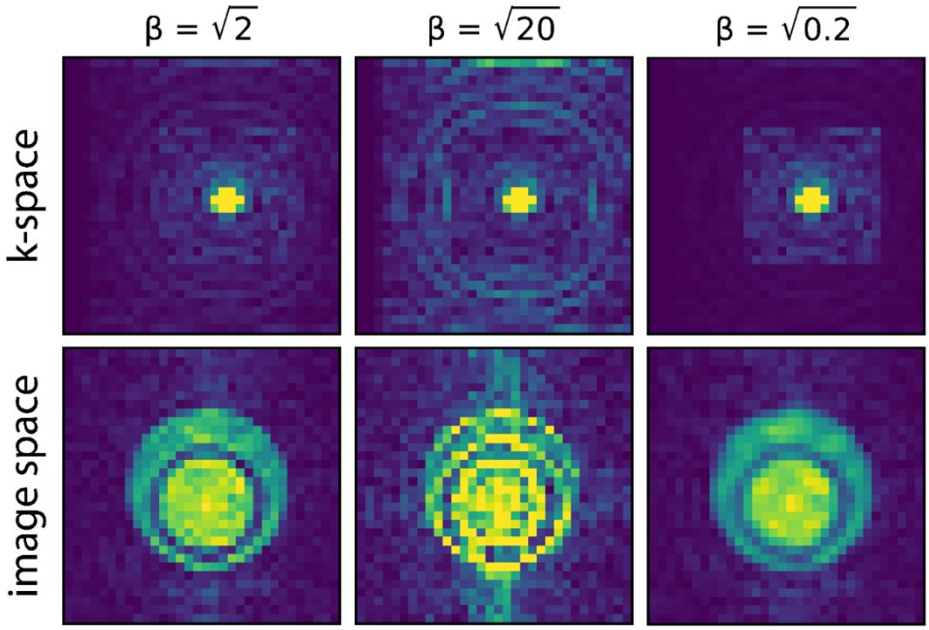

Fig. S4. Effect of the substitution factor on the image reconstruction. Top row: Hybrid k-spaces with keyhole size 16x16, left to right: theoretical, overestimated and underestimated β values. Bottom row: Image reconstruction (by Fourier transform) of the respective k-spaces above.

SI. 3. Stripes as keyholes

In the current implementation, the squared keyhole regions are actually acquired as stripes with N frequency and N/R phase encoding steps. These stripes are trimmed into squares of the desired size of $(N/R)^2$. This ensures that the different frequency encoding steps in the reference and in the keyhole images are acquired at the same time points after excitation and thus eliminates any potential variations in the signal post-processing (e.g., from digital filtering). An additional reason for the acquisition of stripes was to avoid a previously reported[4] shift of k-space data in Bruker MRI data when low matrix sizes (lower or equal to 32x32) are used. The result of this shift is that the first three sampling points of each phase encoding step are significantly underestimated. Merging such flawed keyhole data with the reference k-space data would lead to a discontinuity in k-space signal intensities and thus to image artifacts. The acquisition of stripes and the subsequent trimming of k-space data bypasses this shift problem. For low matrix sizes, the data shift might appear in the fully sampled reference image already. This must be considered in the merging process.

SI. 4. ^{129}Xe flip angle calibration and validation of correct variable flip angle (VFA) implementation

Flip angle (FA) calibration was done by using k-space (magnitude) data from one acquisition with matrix size 32x32 using an adapted 2D FLASH sequence. A constant nominal FA was set to a nominal value of ca. $60°$ (guessed from previous experience). The excitation pulse shape was rectangular, phase encoding (PE) was disabled and the reference power was set to 0.04 W (value guessed from a $90°$ block pulse calibration done in Topspin and calculated for a 1 ms pulse duration). The central six pixels from each k-space line were extracted and then summed, this sum was assigned as the signal value. The trend of the k-space signal against the line number is shown in Fig. S5A.

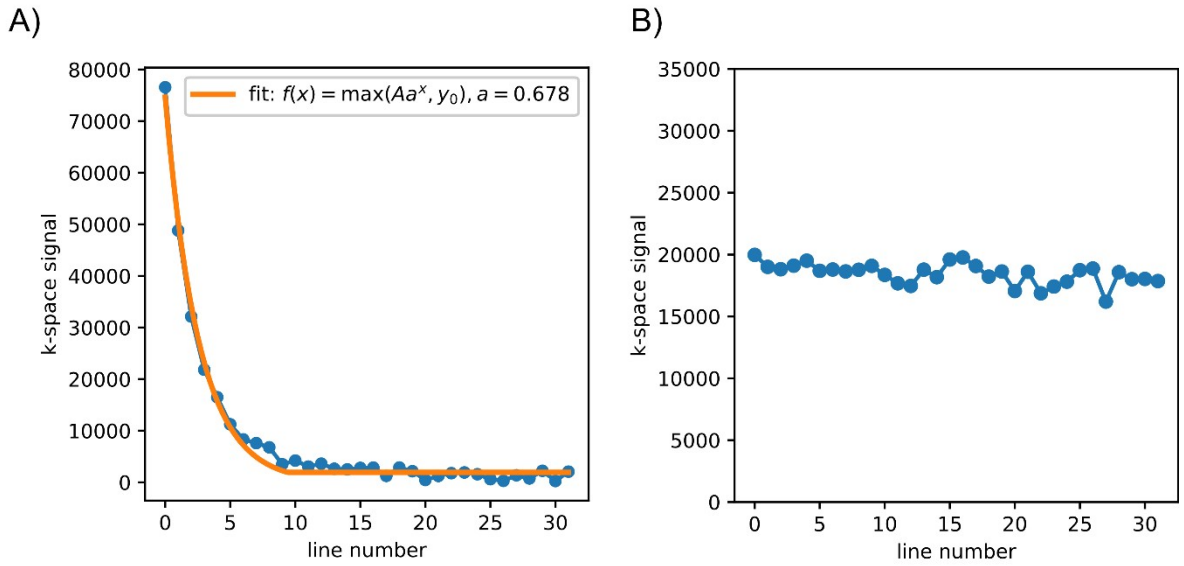

Fig. S5. (A) Signal decay with nominal CFA=60° (blue) and fitting of an exponential function $f(x) = \max\left(A \cdot a^x, y_0\right)$ to this curve (orange; y_0 respects the Rician noise that becomes relevant after ca. 9 excitations). Each signal value is the sum of the six central pixels in the corresponding k-space line. Extraction of the exponent base value from the fit allows to calculate the measured flip angle and correct it. (B) Constant signal with VFA. The constant trend serves as validation of correct VFA implementation.

The theoretical equation for the curve in Fig. S5A:

$$S(n) = M_0 \sin\alpha\left(e^{-TR/T_1} \cdot \cos\alpha\right)^n, \qquad n = 0,1 \ldots N-1$$

(S4)

Where $S(n)$ is signal intensity in the *n*-th line, M_0 is the initial longitudinal magnetization, α is the measured flip angle (with nominal value of 60°), *n* is the line number and *N* is the total number of lines (number of PE steps). Under the assumption that $TR \ll T_1$ ($T_1$of xenon in water at 9.4 T is ca. 100 sec) Eq. S4 simplifies to:

$$S(n) = M_0 \sin\alpha(\cos\alpha)^n, \qquad n = 0,1 \ldots N-1.$$

(S5)

Fitting an exponential function (of the form $f(x) = \max\left(A \cdot a^x, y_0\right)$) to this curve and extracting the value of the exponent base a, provides the measured flip angle ($\alpha = arcos(a)$). The result is $\alpha = 47.34°$ and the fitted curve is displayed in Fig. S5A. This lower than expected α value is compensated by increasing the value of the reference power from 0.04 W to 0.064 W (a factor of $(60°/47.34°)^2 = 1.606$). Next, we repeated the image acquisition and fitting routine to validate we could measure $\alpha = \sim 60°$. Before the fitting routine, the spoiling gradient of the read direction was verified for sufficient strength such that a monotonic decreasing trend appeared for the blue curve in Fig. S5A. Using the adjusted value for the reference power, we changed the flip angle scheme from constant to variable and acquired the k-space data for another image. The rest of the acquisition parameters remained unchanged (especially PE is still disabled). VFA acquisition should provide a constant k-space signal along the lines (refer to VFA section). Fig. S5B shows k-space signal vs. line number with the VFA scheme, as expected the signal is distributed uniformly along the lines. Miscalibration would cause deviation from the constant trend, typically in the form of high signal in the last few lines.

SI. 5. Quantification of SNR increase

Here we study the SNR achieved for images acquired with the proposed CAVKA method. A sample solution containing cryptophane-A mono-acid (CrA-ma; 10 µM in water + 0.2% DMSO) was used. ^{129}Xe Imaging parameters were: excitation pulse shape = sinc, TE = 5.6 ms, TR = 12.2 ms, FOV = 10x10 mm^2, slice thickness = 20 mm, BW = 4 kHz, matrix = 32x32. Smaller matrix sizes for keyhole acquisitions were realized by changing the phase encoding interpolation parameter between 1 (matrix = 32x32) and 8 (matrix = 32x4). SNR is calculated as the mean of the signal ROI over the SD of a comparative noise ROI of 49 pixels (~5% of total numbers of pixels) located in the top left corner of every image (see Fig. S6C). Measurements were done in room temperature (without using the variable temperature unit).

We independently investigated the effect of the keyhole size on signal intensity (Fig. S6A) and the effect of the number of averages on SNR (Fig. S6B). We also studied the combined effect of both approaches (Fig. S6C). All data shown in Fig. S6A were acquired without averaging. Following the calculations in Eq. S3, the signal intensity shows a square root dependency on the undersampling factor. This is shown by the linear function with a slope of 0.5 on a double-

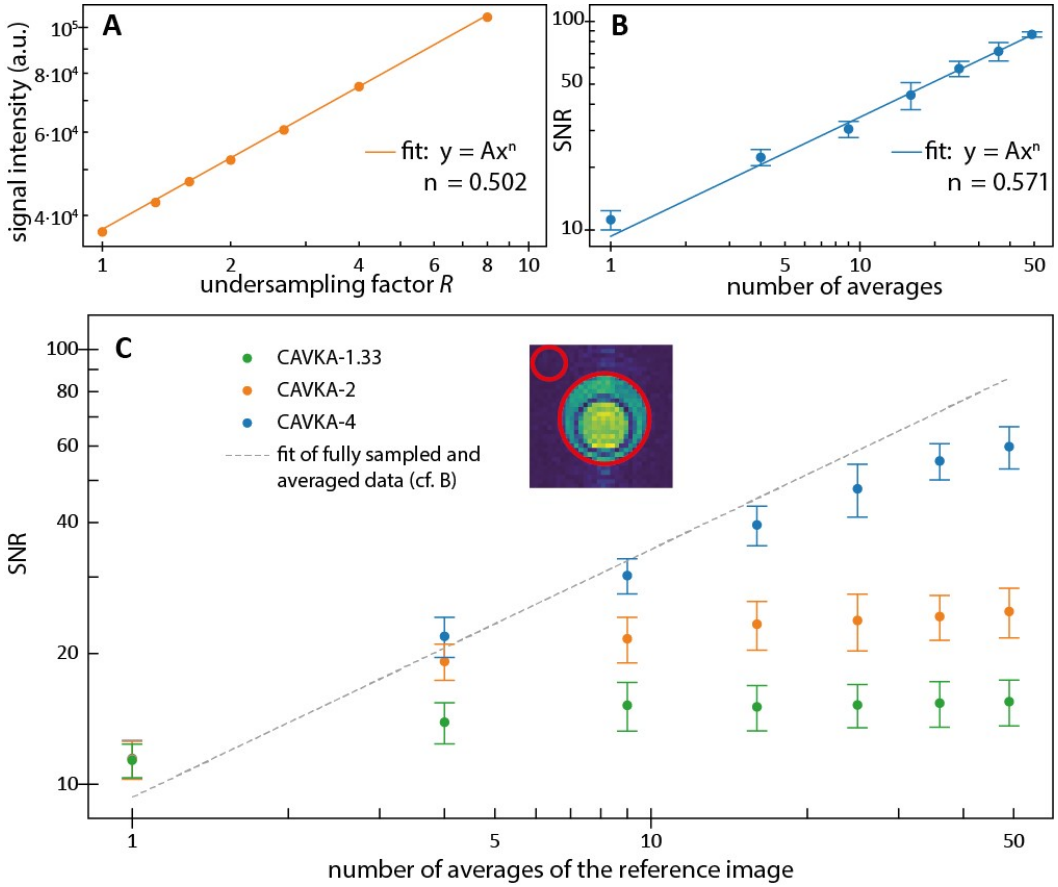

Fig. S6. Signal and SNR dependencies of the CAVKA approach. (A) Signal intensity in non-averaged hybrid image vs. undersampling factor (error bars too small to be displayed). (B) SNR in fully sampled images vs. number of averages. (C) SNR in hybrid images with different combinations of undersampling factors *R* (1.33, 2 and 4) and number of averages of the reference image. All data points represent the mean ± 1 SD values of 10 independent measurements.

logarithmic plot (Fig. S6A). Fig. S6B shows the general effect of averaging on SNR. All data shown in this sub-figure were acquired without using the keyhole approach. As expected, a square root dependency of the SNR on the number of averages is observed. Finally, Fig. S6C shows the combined effect of averaging the reference image (and thus the k-space periphery) and enhancing the signal intensity in the keyhole region (due to the VFA-approach). The plot shows the SNR as a function of the number of averages of the reference image for three different undersampling factors of *R* = 1.33 (green), *R* = 2 (orange) and *R* = 4 (blue). In addition, the linear

fit from Fig. S6B is included (dashed gray line) to show the theoretical SNR values when both, the periphery and the keyhole region, were averaged (at the cost of longer acquisition time). Importantly, the SNR of the CAVKA method increases with increasing undersampling factors and almost reaches the level of the dashed reference line for CAVKA-4. In addition, for a fixed undersampling factor, the SNR increases with increasing numbers of averages of the reference image. This effect is more dominant for higher undersampling factors (and thus smaller keyhole sizes), because larger fractions of the k-space data benefit from averaging the reference image. A possible limiting factor for the undersampling factor/keyhole size could be the capturing of dynamic changes in detailed (small) features of the image or along sharp edges. In this work, dynamic CEST contrast between the two compartments of the phantom was still captured using a 8x8 keyhole size ($R = 4$). This matter was also investigated in a four-compartment digital phantom that has a more complex geometry than the two-compartment phantom, see section S7.

SI. 6. Derivation of CAVKA acceleration factor and ^{129}Xe deliveries saving

^{129}Xe imaging includes the steps of xenon gas delivery (typically 10-15 s) and allowing the bubbles to collapse (typically ≤ 5 s). Their combined time (t_{del}) limits the acceleration factor of the CAVKA acquisition to be approximated as $N_\omega \cdot NA/(N_\omega + NA)$. However, for other applications, where the acquisition time is equal to the total scan time, i.e., the acquisition time is the multiplication of *TR* (the repetition time between two phase encoding steps) with the number of phase encodes and with the number of images and/or averages, a higher acceleration factor can be achieved. This factor is given by $N_\omega \cdot R \cdot NA/(N_\omega + R \cdot NA)$. The formulas are based on a constant *TR* (typically on the order of 10 ms) for all images. t_{sat} is the duration of the saturation pulse (part of the CEST preparation block) and is typically on the order of t_{del}. The derivation is as follows:

a) Acceleration factor for HyperCEST

The acquisition time of a fully sampled and averaged image series is given by

$$t_{fully\ sampled\ and\ averaged} = (t_{del} + t_{sat} + N_{PE} \cdot TR) \cdot NA \cdot N_\omega.$$

For CAVKA, one fully sampled and averaged reference image and N_ω keyhole images (without averages) are acquired. Thus, the total time is given by:

$$t_{CAVKA} = (t_{del} + t_{sat} + N_{PE} \cdot TR) \cdot NA + (t_{del} + t_{sat} + N_{PE}/R \cdot TR\ ) \cdot N_\omega.$$

The acceleration factor is given by the ratio of both acquisition times:

$$\frac{t_{fully\ sampled\ and\ averaged}}{t_{CAVKA}} =$$

$$= \frac{(t_{del} + t_{sat} + N_{PE} \cdot TR) \cdot NA \cdot N_{\omega}}{(t_{del} + t_{sat} + N_{PE} \cdot TR) \cdot NA + \left(t_{del} + t_{sat} + \frac{N_{PE}}{R} \cdot TR\right) \cdot N_{\omega}}$$

$$\overset{TR \ll t_{del}}{=} \frac{(t_{del} + t_{sat} + N_{PE} \cdot TR) \cdot NA \cdot N_{\omega}}{(t_{del} + t_{sat} + N_{PE} \cdot TR) \cdot NA + \left(t_{del} + t_{sat} + \frac{N_{PE}}{R} \cdot TR\right) \cdot N_{\omega}}$$

$$= \frac{(t_{del} + t_{sat}) \cdot NA \cdot N_{\omega}}{(t_{del} + t_{sat}) \cdot NA + (t_{del} + t_{sat}) \cdot N_{\omega}} = \frac{NA \cdot N_{\omega}}{NA + N_{\omega}}$$

The overall behavior of the acceleration factor as a function of the number of averages of the reference image and the extent of the imaging series is shown in Fig. S7.

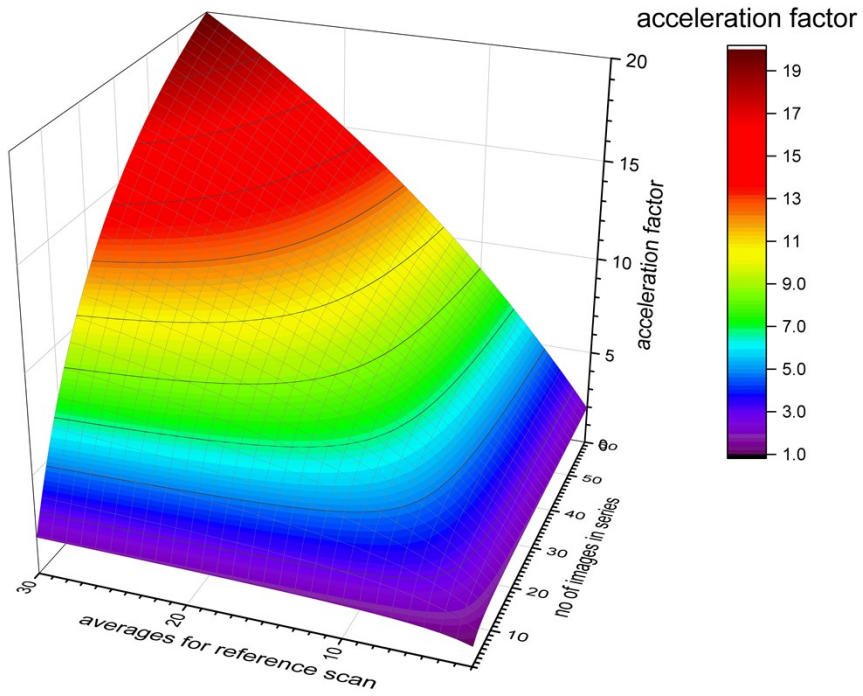

Fig. S7. Dependence of the CAVKA acceleration factor on the number of averages of the reference scan and on the number of images in the series.

This acceleration capability addresses the unfavorable combination of time-consuming steps that is beyond the scope of other undersampling approaches such as compressed sensing[5], deep learning[6] and parallel imaging[7]. These assume the phase encoding steps to be the most time-consuming element and target on reducing their number by subsampling. However, a reduced number of phase encodes would not lead to a meaningful acceleration when a fixed time of hp media delivery and/or magnetization preparation is needed before the readout. When time-consuming pre-encoding steps are needed in each averaging acquisition, only a reduction of averaging steps by reusing a reference image with sharable data along the imaging series dimension provides the desired acceleration. Similarly, as for imaging methods of parallel imaging, CAVKA is a technique that can be used to process undersampled data from different types of pulse sequences. However, the two methods pursue different acceleration approaches and differ by the hardware requirements, namely the multichannel receiver array that is needed in parallel imaging.

b) ^{129}Xe deliveries saving

The number of ^{129}Xe deliveries for a fully sampled and averaged series is $NA \cdot N_\omega$. For CAVKA, however, we acquire one fully sampled and averaged reference image and N_ω keyhole images. The number of deliveries is therefore $NA + N_\omega$. The saving factor is given by the ratio of the number of deliveries:

$$\frac{NA \cdot N_\omega}{NA + N_\omega}$$

c) Acceleration factor for other types of imaging series

For generality, we assume an application without a pre-readout preparation block. The calculation remains the same as for HyperCEST but t_{del} and t_{sat} can be omitted (no delivery and saturation times):

$$\frac{t_{fully\ sampled\ and\ averaged}}{t_{CAVKA}} = \frac{N_{PE} \cdot TR \cdot NA \cdot N_\omega}{N_{PE} \cdot TR \cdot NA + N_{PE}/R \cdot TR \cdot N_\omega} = \frac{NA \cdot N_\omega \cdot R}{R \cdot NA + N_\omega}$$

Applying CAVKA to acquire an image series with the same size and number of averages like the one needed for the spectral data shown in Fig. S8 would result in acceleration factor of ~17 in this application instead of just ~7 in HyperCEST.

SI. 7. Comparison of z-spectra from CAVKA and conventional acquisition with averaging

We applied CAVKA to acquire a CEST image series using hyperpolarized ^{129}Xe and CrA-ma as a well characterized HyperCEST agent. For CEST preparations, a rectangular pulse with amplitude B_1 = 15 µT and duration t_{sat} = 10 s was used. Saturation was applied at 35 offsets (-361, -361, -361, -149, -144, -139, -138, -137, -136, -135, -134, -133, -132, -131, -130, -129, -128, -127, -126, -125, -120, -115, -90, -45, -12, -9, -6, -3, -1.5, 0, 1.5, 3, 6, 9 and 12 ppm) relative to ^{129}Xe in water. The first three offsets were used as dummies to stabilize the gas delivery and were not included in the data processing. Fig. S8 shows the z-spectra from a data set acquired using CAVKA-4 with 9 averages of the reference image (blue) compared to a fully sampled and 9-times averaged data set (orange). The inlay visualizes the corresponding acquisition times of 21 min and 149 min for the CAVKA-4 and the fully sampled and averaged acquisition, respectively. The nature of hyperpolarized nuclei demands their redelivery for each image in the series and therefore not only for the different offsets, but also for each averaging acquisition. This is due to the fact that the non-equilibrium magnetization is used up after each acquisition. Consequently, the CAVKA approach of acquiring one averaged reference image and (partially) reusing it for the entire image series reduces the number of gas deliveries from 315 to 44 and thus the acquisition time by ~86%. The z-spectra in Fig. S8 show excellent agreement between conventional (fully sampled and averaged) and CAVKA-based acquisitions and thus demonstrate the potential of the proposed CAVKA method to accelerate the acquisition of image series (like in CEST MRI) without sacrificing image or data quality.

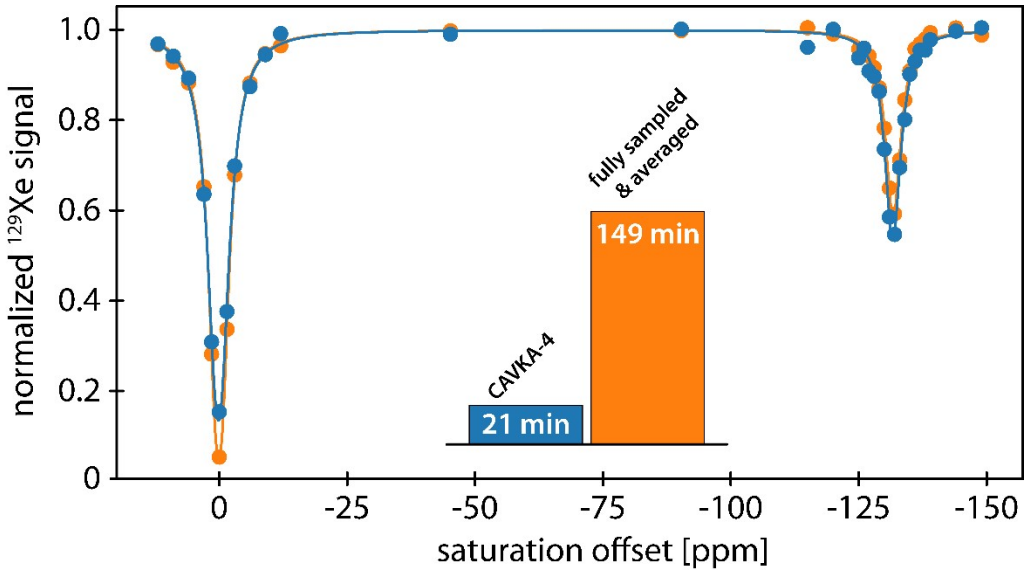

Fig. S8. HyperCEST z-spectra of CrA-ma acquired using CAVKA-4 method and conventional imaging with averaging. Data points represent ROI-averaged and normalized signal intensities. The almost complete overlap of the spectra shows the reliability of the CAVKA method and yet with a 7-fold reduction of the acquisition time.

SI. 8. Digital phantom simulation to study the reuse of high frequency information in a CEST acquisition and the error of this reuse in ROI-based z-spectra

The sharing of k-space data that carries information on the edges of each sample tube may raise concerns about potential artefacts in spectra that are derived from ROIs. We thus investigated this aspect with a "digital phantom" that comprises multiple compartments of different shape (i.e. a more complex geometry than in our application) to test the method for robustness. The utilized digital phantom (size 256x256) is inspired by the Shepp-Logan virtual phantom[8] and comprises four compartments. Signal intensities of a Z-spectrum were assigned to each pixel in the different compartments. These z-spectra (41 offsets between 100 ppm and 140 ppm) are based on numerical simulations following the Bloch-McConnell (BMC) equations[9] for two pools (bulk and CEST). The outer compartment (Comp. 1) maintains a constant (non-CEST responsive) signal and the other compartments were carefully designed to provide different combinations of on-resonant (120 ppm) and off-resonant (100 or 140 ppm) contrast: Compartments 2 and 3 have the same on-resonant contrast, but unlike compartment 2, compartment 3 does not have off-resonant contrast at all. Compartment 4 has an on- and off-resonant contrast, however, both are lower compared to compartment 2. These differences in on- and off- resonant contrasts were chosen to test the performance of CAVKA under different scenarios and were realized by adjusting the relative pool size fractions of the CEST pool to 0.4%, 0.5% and 0.1% for compartments 2, 3 and 4, respectively. Additionally, the corresponding pool sizes of the bulk pool were set to 0.8, 1 and 0.9. Other simulation parameters were: T1/T2 of bulk pool = 2/0.2 s, T1/T2 of CEST pool = 2/0.03 s, CEST resonance frequency = 120 ppm, exchange rate with the bulk pool = 500 Hz, saturation power B_1 = 5 µT, saturation duration t_{sat} = 20 s. CAVKA images were reconstructed for undersampling factors *R* = 2, 4, 8, 16, 32, and 64. For the reference image, 16 averages were used. The averaging was mimicked in a three-step process (see section S8) to respect the different noise conditions between the keyhole and the periphery. Keyholes were created using the fully-sized k-space, which was multiplied by $\sqrt{R}$ (following Eq. S3) to simulate the VFA signal enhancement, followed by the addition of noise and finally cutting out the center (according to *R* value). Hybrid k-space data were constructed in the same way as the experimental data. The simulated data is available at http://doi.org/10.5281/zenodo.4883621.

The keyhole method is prone to loss of image details when excessive undersampling is applied. Fig. S9a compares between a CAVKA-16 image (including a reference image of 16 averages) and a fully sampled image simulated to be acquired with the same number of averages. *R* = 16 is a more extreme application of the method than in our experimental data to validate the robustness of CAVKA. This comparison is done for the off-resonant and on-resonant (120 ppm) case. Whereas the off-resonant CAVKA image shows no artefacts at all (Fig. S9a bottom left), the on-resonant one exhibits artefacts in the form of blurred edges of the inner compartments (Fig. S9a bottom right). To investigate these artefacts as a function of the undersampling factor, error maps for undersampling factors between 2 and 64 were calculated. These maps (Fig. S9b) show the pixel-wise deviations of the on-resonant CAVKA images from the simulated BMC-based

images without noise. As expected, the errors increase with increasing undersampling factors and are most pronounced for compartment 3, which does not have any off-resonance contrast and is thus the most challenging one for the proposed CAVKA method. However, up to an undersampling factor of 16, the errors are restricted to the edges of the compartments. For higher *R*-values, distortions start to appear and the errors are not limited to the edges of the compartments anymore. The overall increased deviations in the CAVKA-2 error map are the result of high noise values in the relatively large keyhole region when a small undersampling factor is chosen. We further investigated the influence of these distortions on ROI-based z-spectra for *R*=16 and 16 averages of the reference image. Fig. S9c shows the ROI-averaged z-spectra of compartments 2 (blue), 3 (orange) and 4 (green). The dashed lines correspond to the CAVKA data, the solid lines to the simulated BMC data and the dashed-dotted lines show their difference. Despite including pixels close to the compartment edges (ROIs were identical to the compartments shapes), differences in the spectra occur only at the on-resonant frequency. In agreement with the error maps shown in Fig. S9b, the largest deviations are observed for compartment 3.

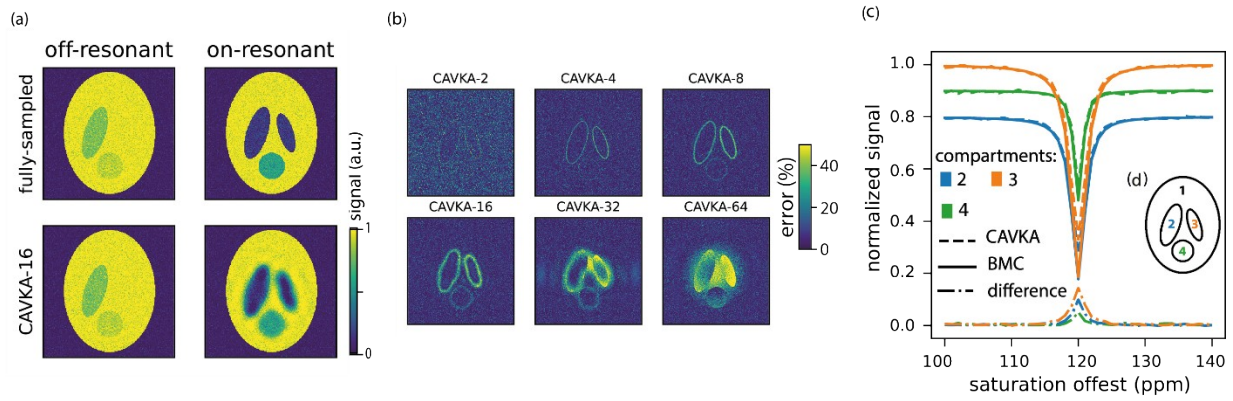

Fig. S9. Performance of the CAVKA method on a digital phantom (matrix size 256x256) with different CEST-responsive areas. a) Off- and on-resonant CEST images illustrating artefacts in CAVKA images. CAVKA images were normalized (divided by $\sqrt{R}$) to allow comparison. Off-resonant images retain sharp edges, on-resonant images experience blurring for the edges of the CEST-responsive areas. b) Error maps for CAVKA images for undersampling factors between 2 and 64. The error maps were calculated by subtracting CAVKA images from noise-free BMC-based images followed by normalization. c+d) CEST compartments and CEST spectra derived from the respective ROIs in the CAVKA-16-reconstructed images (using 16 averages for the reference image) and from BMC-simulated reference spectra.

The geometry of the digital phantom was chosen to be more complex and, in this scenario, the limit for the keyhole size was found to be around 16x16. However, this corresponds to an undersampling factor of *R*=16 already and shows that the maximal achievable undersampling

factor highly depends on the geometry of the measured object and the matrix size of the reference image. In general, objects with complex geometry or contrast pattern demand for larger keyhole matrix sizes. Furthermore, the simulations revealed that the difference in contrast between the reference image and the keyhole image is a crucial point for the CAVKA approach that should be considered when adjusting the undersampling factor for a specific scenario.

SI. 9. Noise handling for averaging in synthetic data of digital CEST phantom

The averaging in simulated data of the digital phantom was mimicked in a three-step process to respect the different noise conditions between the keyhole and the periphery. In the first step, normally distributed real-valued noise with zero mean and standard deviation = 1/3 was added to a noise-free image (the first in the z-spectrum imaging series). This was repeated to obtain a stack of 500 different noise-carrying images that are afterwards transformed to (complex) k-space. In a second step, a subtraction of the non-noisy data from each element of the noisy data stack yields an isolated noise data stack (500 elements) in k-space. In the third step, the average of up to 49 randomly selected and complex-valued sets from the noise data stack was added to the noise-free data to create the k-space stack with a pre-selected number of (noise) averages.

SI. 10. Lorentzian curve fitting to HyperCEST z-spectra

Exponential Lorentzian curves were fitted to the measured z-spectra by using the function:

$$y(x) = max\left(M_0 e^{-\left[\frac{\lambda_{on-res1}\left(\Gamma_1/2\right)^2}{\left(x-x_{c1}\right)^2+\left(\Gamma_1/2\right)^2}+\frac{\lambda_{on-res2}\left(\Gamma_2/2\right)^2}{\left(x-x_{c2}\right)^2+\left(\Gamma_2/2\right)^2}\right]},\sigma\right).$$

σ respects the Rician noise (same as in section SI. 3) and it is the residual signal value in the case of complete saturation. The first function in the *max* argument is a superposition of two Lorentzians; the first one (parameters with index 1) models the direct saturation (i.e., saturation of the free xenon pool), and the second one (parameters with index 2) models the CEST saturation. λ_{on-res}, Γ, x_c denote the maximum (i.e., on-resonant) depolarization rate, FWHM, and the center of each peak, respectively, and M_0 denotes the baseline value (magnetization value without saturation). Fitting was done initially to each of the non-normalized spectra to extract the value of M_0. In such plots, the Rician noise level is identical in both compartments but M_0 typically differs in the two ROIs. Next, each spectrum was normalized by dividing all of its data points by the value of M_0. This was then used to perform a second fitting to each of the normalized spectra. $M_0 = 1$ is then obtained for both compartments but the area with originally lower starting magnetization exhibits the higher noise level σ. If necessary, like in the case of CB7 + cadaverine in Fig. 6a, fitting of the spectrum was done with only one Lorentzian as now systematic signal could be identified at -95 ppm offset.

SI. 11. Screening acquisitions for quick validation and to refine concentrations

Before obtaining more detailed spectra at certain host:guest ratios, some quick screens have been performed to obtain some first orientation. This applies to the results shown in Fig. 5-6, but also to quickly exclude any significant interaction of **1** with CB6. These screens were done by obtaining coarse HyperCEST spectra with a relative short list of offsets (saturation frequencies) to save time.

The experiments in Fig. S10 and S11 were done as imaging experiments in a single (one-compartment) phantom where all samples had a volume of 1.5 ml. Imaging was done with CFA = 20° and with 9 saturation frequencies offsets (−360, −360, −360, −121, −95, −69, −40.6, 0 and 40.6 ppm) relative to ^{129}Xe in water (first three offsets were acquired as dummy scans to stabilize the gas flow and were omitted in data processing). The rest of the acquisition parameters were as detailed in the experimental section. These are not CAVKA acquisitions; neither averaging nor VFA was used. Since only single phantom was used (one ROI), the image quality was sufficient for signal extraction.

After observing that the blocker **1** did not sufficiently suppress the CEST response from a CB7 sample (see Fig. 4a), it was considered that the CEST response is only from a CB6 impurity in CB7 and the assumption that **1** is probably too big to be included in CB6. We therefore tested the effect of **1** directly on CB6 by comparing the z-spectra of 10 μM CB6 without and with the blocker **1** at 1:1 ratio. This concentration of CB6 was chosen as it provides appropriate CEST response that can be tested for blocking. Fig. S10 shows the results. No blocking effect of **1** on CB6 was detected. The two spectra were acquired from imaging experiments in a single phantom by first measuring just CB6 and repeating the measurement after the addition of **1**.

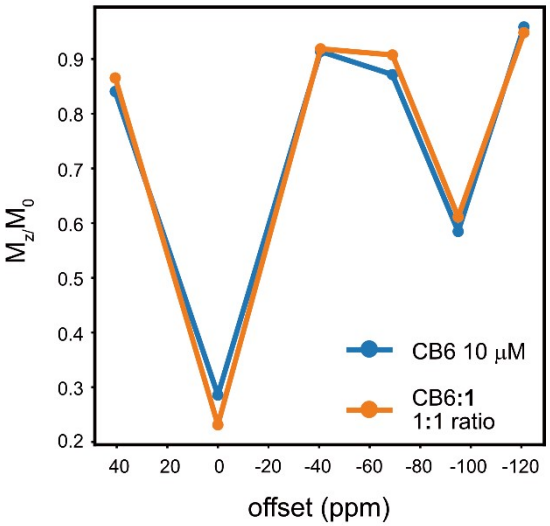

Fig. S10. Z-spectra of 10 μM CB6 with (orange) and without (blue) the guest **1** at 1:1 ratio.

For estimating the CB6 concentration that provides a similar CEST response as from the nominal 50 μM CB7 sample, CB6 aqueous solutions with concentrations of 0.5, 1 and 1.5 μM were prepared. Their HyperCEST spectra were measured and compared to the spectrum of CB7. Fig. S11a shows the results. The CEST response (signal dip at -95 ppm) increases when the CB6 concentration increases and 1.5 μM CB6 achieves a comparable response as from CB7 (only as a first approximation, more exact quantification appears in the main text). Thus, this concentration was chosen for the experiment shown in Fig. 5b.

In the same manner, a first approximation for the minimal putrescine concentration that fully blocks the CEST response from 50 μM CB7 was determined. Solutions of 50 μM CB7 and putrescine in concentrations of 0.5, 1 and 4 μM (CB7:**3** at ratios of 100:1, 50:1 and 12.5:1) were prepared. Their HyperCEST spectra were measured and compared to the spectrum of CB7 only. Results appear in Fig. S11b. The suppression of the CEST response increases when the putrescine concentration increases and 4 μM putrescine achieves an almost full blocking. This putrescine concentration was then used in the experiment shown in Fig. 6b.

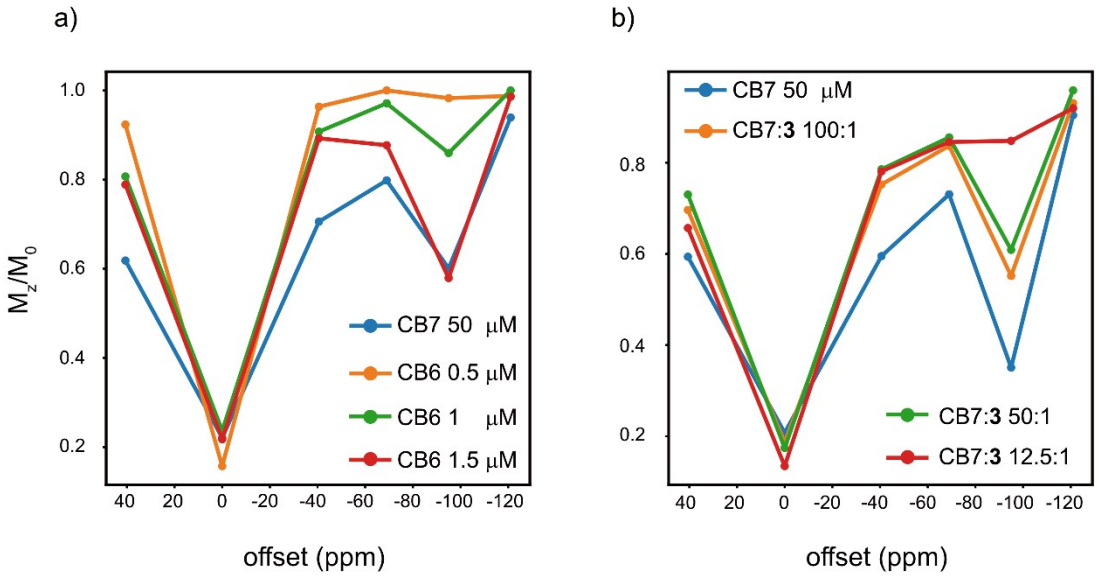

Fig. S11. Screening suitable concentration ranges. a) Refining the CB6 concentration that provides similar CEST response as from 50 μM CB7. b) Refining the putrescine concentration that fully suppresses the CEST response from 50 μM CB7. Data points represent signals from ROI averages obtained from images.

SI. 12. Exclusion of Xe interactions at 100-fold dilution

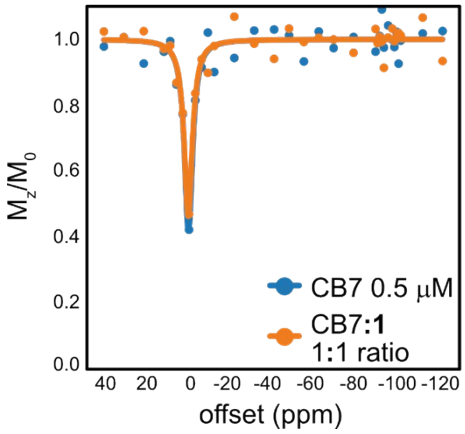

Fig. S12. CAVKA-derived z-spectra for diluted samples of CB7 show no signs of Xe binding or labile interaction.

SI. 13. Fitting results for quantitative analysis of z-spectra

1. Fitting results for spectra in Fig. 5a: 50 µM CB7 vs. 5 µM CB6

	chemical shift			
	CB7 sample		CB6 sample	
	ppm	Error	ppm	error
direct saturation	-0.5	0.1	-0.44	0.08
CEST peak	-94.6	0.2	-95.1	0.1
difference	-94.1	0.2236068	-94.66	0.12806248

	peak width (FWHM)			
	CB7 sample		CB6 sample	
	ppm	error	ppm	error
CEST peak	14.1	0.6	14.0	0.4

	depolarization rate single phantom			
	CB7 sample		CB6 sample	
	λ_2	error	λ_2	error
CEST peak	0.02055	0.0005	0.02232	0.0004
factor λ_2 for CB7 vs. CB6	0.92069892	0.02782218		
nominal CB6 reference	5	µM		
predicted CB6 impurity	4.60349462	µM		
error	0.13911089	µM		

2. Fitting results for spectra in Fig. 5b: 50 µM CB7 vs. 1.5 µM CB6

	chemical shift			
	CB7 sample		CB6 sample	
	ppm	error	ppm	error
direct saturation	-1.7	0.6	-0.06	0.09
CEST peak	-95.0	0.3	-94.0	0.5
difference	-93.3	0.67082039	-93.94	0.50803543

	peak width (FWHM)			
	CB7 sample		CB6 sample	
	ppm	error	ppm	error
CEST peak	13.8	1.8	15.9	2.4

	depolarization rate double phantom			
	CB7 sample		CB6 sample	
	λ_2	error	λ_2	error
CEST peak	0.0285	0.0016	0.011	0.0007
factor λ_2 for CB7 vs. CB6	2.59090909	0.21986617		
nominal CB6 reference	1.5	µM		
predicted CB6 impurity	3.88636364	µM		
error	0.32979925	µM		

The widths of the CEST response are very similar and overlap within 1 SD . This is another strong indication that both host systems provide the same rate k_{BA} to release Xe. The CB6 sample was in the outer compartment that could potentially see slightly higher B_1 saturation field and thus produce a minor line broadening compared to the inner compartment. The B_1 inhomogeneity of this type of coil was investigated in the SI of Ref. [10] The SD of B_1 was ca. 5% for such a setup and this might at least partially explain a somewhat broader signal from the outer compartment.

3. Fitting results for spectra in Fig. 6b: blocking the signal from 50 µM CB7 with 4 µM **3**

	depolarization rate double phantom			
	CB7 sample		CB7 + 4 µM Put	
	λ_2	error	λ_2	error
CEST peak	0.02525	0.00133	0.00248	0.0005
blocking factor in %	90.1782178	2.04666324		
nominal concentration **3**	4	µM		
predicted CB6 impurity	4.43566096	µM		
error	0.1006707	µM		

References:

1 J. Döpfert, C. Witte and L. Schröder, *ChemPhysChem*, 2014, **15**, 261–264.

2 A. Lakshmanan, G. J. Lu, A. Farhadi, S. P. Nety, M. Kunth, A. Lee-Gosselin, D. Maresca, R. W. Bourdeau, M. Yin, J. Yan, C. Witte, D. Malounda, F. S. Foster, L. Schröder and M. G. Shapiro, *Nature Protocols*, 2017, **12**, 2050–2080.

3 C. Witte, M. Kunth, F. Rossella and L. Schröder, *The Journal of Chemical Physics*, 2014, **140**, 084203.

4 C. Cobas, NMR Analysis, Processing and Prediction, http://nmr-analysis.blogspot.com/2008/02/why-arent-bruker-fids-time-corrected.html, (accessed 7 November 2019).

5 M. Lustig, D. Donoho and J. M. Pauly, *Magnetic Resonance in Medicine*, 2007, **58**, 1182–1195.

6 C. M. Hyun, H. P. Kim, S. M. Lee, S. Lee and J. K. Seo, *Phys. Med. Biol.*, 2018, **63**, 135007.

7 A. Deshmane, V. Gulani, M. A. Griswold and N. Seiberlich, *Journal of Magnetic Resonance Imaging*, 2012, **36**, 55–72.

8 L. A. Shepp and B. F. Logan, *IEEE Transactions on Nuclear Science*, 1974, **21**, 21–43.

9 H. M. McConnell, *The Journal of Chemical Physics*, 1958, **28**, 430–431.

10 M. Kunth, C. Witte and L. Schröder, *The Journal of Chemical Physics*, 2014, **141**, 194202.